Effects of the Solution Treatment on Microstructural Evolution, Mechanical Properties, and Fracture Mechanism of Nickel-Based GH4099 Superalloy

Guangsheng Xu[1,2], Chuan Wu[3], Zhenhua Liu[1], Yilong Wang[1], Zhanying Zhang[1], Yun Li[1], Ping Hu[2]

[1]Engineering Research Center of High-Performance Aerospace Materials and Devices, Universities of Shaanxi Province, Shaanxi Polytechnic Institute, Xianyang, China
[2]Xianyang Key Laboratory of New power and Intelligent Microgrid System, Xianyang, China
[3]National-Local Joint Engineering Laboratory of Intelligent Manufacturing Oriented Automobile Die and Mould, Tianjin University of Technology and Education, Tianjin, China
Email: xuguangshengss@163.com

Abstract

Grain growth, mechanical properties, and fracture mechanism of nickel-based GH4099 superalloy are investigated using heat treatments, tensile tests, optical microscopy (OM), and scanning electron microscopy (SEM) with energy dispersive X-ray spectroscopy (EDS). The OM observation shows that the matrix grains (γ-grains) undergo an apparent growth during the solution treatment. The grain size diameter increases from 100 to 174 μm when the solution temperature rises from 1100˚C to 1160˚C for 30 min. When the holding time increases from 15 to 60 min at 1140˚C, the grain size diameter increases from 140 to 176 μm, indicating that the γ-grain growth is more sensitive to temperature than time. Standard deviation, S_v, and the grain size distribution are utilized to characterize the microstructural uniformity. To predict the grain size more accurately, we develop the grain growth kinetics and find that the growth index is close to 5. The yield strength ($R_{p0.2}$), tensile strength (R_m), and ductility (A_f) are also measured. It is found that the effect decreases in the order cooling rate, solution temperature, time. $R_{p0.2}$ reduces by 47% with the increase in the cooling rate from 1˚C to 8000˚C/min, while both strength and ductility exhibit little changes with time. The SEM results show that the fracture surfaces have typical mixed brittle and ductile characteristics when specimens are subjected to water quenching and air cooling. However, a complete brittle fracture occurs under furnace cooling conditions. The EDS analysis indicates that the brittle γ' (Ni₃Ti) phase precipitates around

the γ-grain boundary during the slow cooling process, which is the main factor yielding the complete brittle fracture. Finally, the optimal solution treatment scheme for the GH4099 superalloy is proposed—a temperature of 1140˚C for 30 min followed by air cooling.

Keywords

Microstructural Evolution, Mechanical Properties, Fracture Mechanism, GH4099 Nickel-Based Superalloy

1. Introduction

GH4099 is a typical nickel-based superalloy, which is strengthened mainly by a solid solution of chromium (Cr), tungsten (W), molybdenum (Mo), and cobalt (Co), and second phase precipitation of γ' (Ni_3(Al, Ti)), γ" (Ni_xNb), δ (Ni_xNb), Laves phase, and carbides [1] [2]. GH4099 superalloy exhibits good high-temperature strength, excellent corrosion resistance, and high oxidation resistance. It has been widely used in aerospace engineering and thermal and nuclear power generation to manufacture structural components, such as turbine disks, blades, and engine shafts [2] [3].

As already well established, the mechanical properties of nickel-based superalloys are strongly dependent on their final microstructures, where fine and uniform microstructures are especially beneficial for the improvement of fatigue resistance and mechanical strength [4] [5] [6] [7]. In general, hot working and subsequent heat treatments effectively enhance nickel-based superalloys' microstructural and mechanical properties [8].

Different microstructural evolution mechanisms, such as work hardening, dynamic recovery, and recrystallization, may occur during hot working, which have a significant effect on the final microstructures [9]. After hot working, an appropriate heat treatment scheme is necessary to induce microstructural changes, improve the mechanical properties, and remove the residual stress and micro-defects [5]. However, final microstructures may be altered and deteriorated if the heat treatments are not properly selected. For instance, when a nickel-based superalloy was solution-treated at a relatively high temperature, the γ, γ' phase and carbides may precipitate, and microstructural coarsening may occur, largely enhancing the strength and reducing the ductility and creep properties [10]. Moreover, the δ- and Laves phases can precipitate around grain boundaries of the matrix during a slow cooling stage, yielding micro-defects that act as crack nucleation sites. Therefore, it is necessary to investigate the microstructural evolution and mechanical properties of nickel-based superalloys under different heat treatments to obtain desired microstructures and properties of the nickel-based superalloy parts.

Many studies were performed to assess the microstructural evolution and mechanical properties of typical nickel-based superalloys. Mahboobeh *et al.* [11]

studied the effect of the solution treatment on creep properties of Inconel-713C superalloy and found that the solution treatment at 1200°C for 1 h decreased creep rupture, while the effect is negligible in the case of aging at 930°C for 16 h due to the precipitation of NbC carbides and the coarsening of γ' particles. Zhao *et al.* [12] investigated the coarsening and age-hardening behavior of a novel nickel-based superalloy and showed that the alloy's microhardness decreased significantly with the aging temperature. Ceena *et al.* [8] explored the microstructural evolution and mechanical properties of Haynes 282 superalloy subjected to different heat treatments and determined good room temperature strength and ductility obtained by a standard two-step aging because of the presence of fine-grain boundary carbides and intragranular γ' phase. In contrast, the strength and ductility were significantly reduced upon the solution treatment at 1120°C because of interconnected grain boundary carbides and coarse intragranular γ' phase. Chen *et al.* [13] reported that an annealing treatment could effectively improve the microstructural homogeneity due to the static recrystallization. Masoumi *et al.* [14] determined the kinetics of γ' size and volume fraction of an advanced nickel-based superalloy AD730^{TM} during solution treatment. The authors disclosed the underlying mechanisms and developed a model to describe the dissolution and coarsening processes. Mostafaei *et al.* [15] studied the effect of solution and aging treatments on the microstructural and mechanical properties of a nickel-based superalloy. They showed that intermetallic phases, such as Ni_3Nb and $Ni_2(Cr, Mo)$, and carbides, such as NbC and $Cr_{23}C_6$, could form during the aging stage, simultaneously increasing micro-hardness and tensile strength and decreasing ductility.

Although many studies have been conducted to investigate the microstructural evolution and mechanical properties of nickel-based superalloys during heat treatments, the effect of solution conditions on the microstructural evolution, mechanical properties, and fracture mechanism of a GH4099 superalloy was not investigated in detail. Particularly, the intrinsic relationship between solution treatments, microstructural evolution, mechanical properties, and fracture mechanism is still elusive.

In this study, the solution treatments of a GH4099 superalloy at different temperatures, times, and cooling rates were conducted, followed by uniaxial tensile tests. The microstructural evolution was characterized by optical microscopy (OM). The formed precipitates were analyzed by energy-dispersive X-ray spectroscopy (EDS), while the fracture surface was examined using scanning electron microscopy (SEM). The mechanical properties, such as yield strength, tensile strength, and failure elongation, were determined. The effect of solution conditions on the microstructural evolution, mechanical properties, and fracture mechanism was discussed, and the optimum solution temperature, holding time, and cooling method of the GH4099 superalloy were identified. This study aims to provide an experimental basis for optimizing heat treatment schemes toward desired microstructures and final properties for thin-walled complex components of GH4099 superalloy.

2. Materials and Experiments

GH4099 superalloy (Manufactured By WST) used in the present work consisted (in wt%) of 0.06 carbon (C), 18.5 chromium (Cr), 4.0 molybdenum (Mo), 7.0 cobalt (Co), 6.0 tungsten (W), 2.3 aluminum (Al), 1.16 titanium (Ti), 0.14 other elements, and the nickel balance.

The GH4099 superalloy was subjected to various solution treatments followed by different cooling methods to assess the microstructural evolution. Detailed solution treatment procedures are shown in Table 1. After the solution treatments, standard tensile specimens, Figure 1, were cut from the solution-treated material using electrical discharge machining. The tensile tests were conducted on an MTS810 machine according to GR/T 228-2002 standard. Yield strength ($R_{p0.2}$), tensile strength (R_m), and failure elongation (A_f) were determined. Two specimens were adopted to evaluate the properties for all solution conditions.

The microstructural evolution was examined using an OLYMPUS/PMG3 optical microscope. Metallographic samples were mechanically polished according to metallographic procedures and chemically etched with a solution of 5.0 ml H_2SO_4 + 80 ml H_2O + 150 ml HCl + 20 g $CuSO_4·5H_2O$, of those reagents are of analytical grade and deionized water. The fractography was performed using a Zeiss Sigma500 scanning electron microscope to identify the fracture mechanism of the GH4099 superalloy. The EDS analysis was used to characterize the precipitates at the grain boundaries.
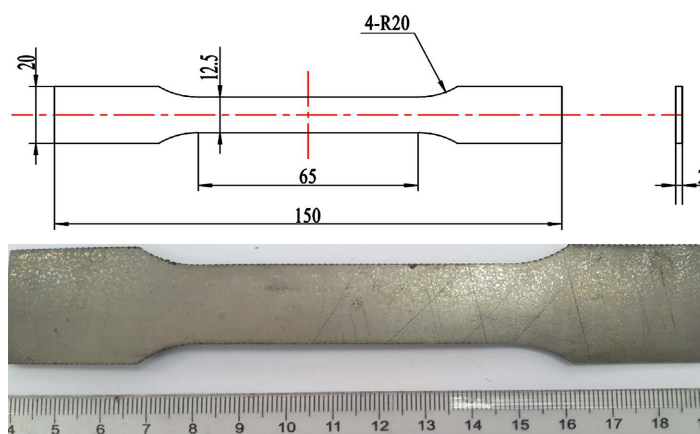

Figure 1. Schematic drawing of tensile specimen (Units: mm).

Table 1. Aging treatment procedures.

Temperature (°C)	Time (min)			
	15	30	45	60
1100	√	√	√	√
1120	√	√	√	√
1140	√	√	√	√
1160	√	√	√	√

3. Results and Discussion

3.1. Microstructural Evolution

The initial microstructure of the GH4099 superalloy before the solution treatment is shown in **Figure 2**. The microstructure is homogeneous, with a grain diameter of approximately 30 µm.

The GH4099 superalloy was solution-treated at temperatures from 1100˚C to 1160˚C for 30 min, followed by air cooling. At the holding stage, the size and distribution of the γ-phase grains change with time, which can directly determine the mechanical properties of superalloy. Thus, it is important to investigate the microstructural evolution under different solution treatments [14]. The optical micrographs of the material, **Figures 3(a)-(d)**, indicate that the microstructure is very sensitive to solution temperature. Comparing to the initial structure, the microstructure becomes coarse, *i.e.*, the grains grow rapidly at higher solution treatment temperatures. The grain size increases from 100 µm at 1100˚C to 174 µm at 1160˚C. Some small grains are locally dispersed along the grain boundaries, and they become increasingly small until they disappear, indicating that relatively large grains grow at the cost of these small grains. When the solution temperature increases to 1120˚C (**Figure 3(b)**), the size of matrix grains becomes large. However, the grain size varies little with a further time increase (**Figure 3(c)** and **Figure 3(d)**), indicating that the growth rate is slow at a fairly high temperature. This tendency has also been observed in the work of Chen *et al.* [5].

The fraction of grains with a size smaller than 10 or 200 µm decreases gradually with temperature, and the grain size becomes nearly equal to the average value. The microstructures become increasingly uniform with temperature. It is generally considered that grain growth is a thermal activation process controlled by atom diffusion. The grain growth process can be described as follows:

$$\Delta r = v \Delta t \tag{1}$$

where Δr is the increment of diameter during Δt, v is grain boundary migration that can be written as follows:
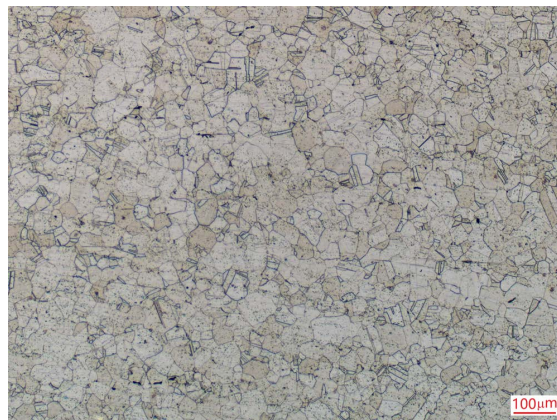

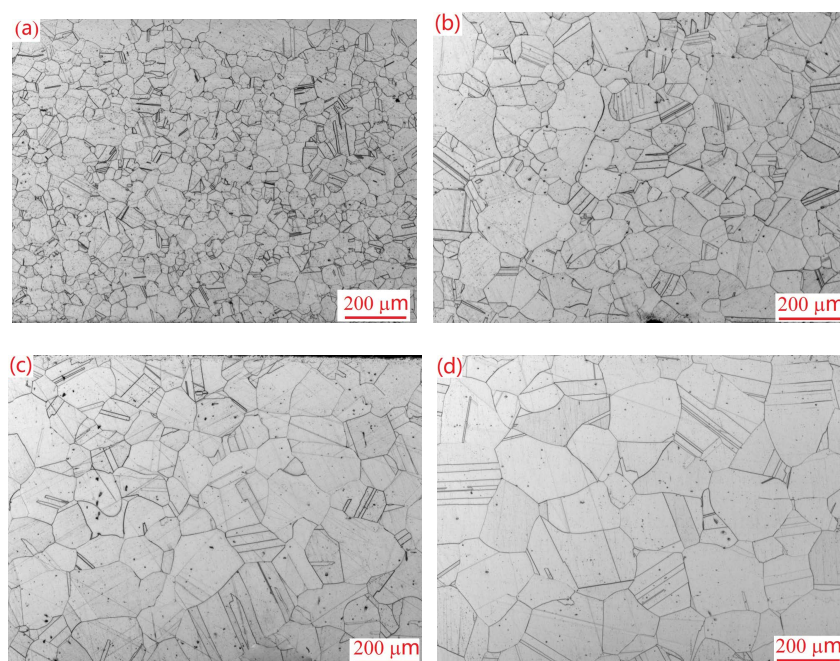**Figure 2.** Initial microstructure of the GH4099 superalloy before the solution treatment.

Figure 3. Microstructural evolution of the GH4099 superalloy solution-treated at temperatures of (a) 1100, (b) 1120, (c) 1140, and (d) 1140 for 30 min.

$$v = M_0 \exp\left(-\frac{Q_{act}}{kT}\right) P \qquad (2)$$

where M_0 and k_B are material constants, Q_{act} is the apparent activation energy of grain boundary migration, and P is the driving force for grain growth. Equation (2) implies that high annealing temperatures can promote the grain boundary migration rate. Thus, the grains become noticeably coarse at relatively high annealing temperatures. **Figure 4** shows the microstructural evolution of the GH4099 superalloy solution treated at 1140˚C for different times. The grain size does not change significantly compared to that in **Figure 3**. The average grain diameter increases from 140 to 176 μm for a time interval from 15 to 60 min at 1140˚C, respectively.

The variation of microstructure uniformity (MU) with the solution treatment time is depicted in **Figure 5**. The MU is represented by the standard deviation ($S_v = \sqrt{\dfrac{1}{N}\sum_{i=1}^{N}\left(d_i - \bar{d}\right)^2}$) of the average γ-phase grain size. **Figure 5(a)** shows that the MU decreases when the time is less than 45 min, but it begins to increase at longer times, indicating that the microstructure becomes nonuniform, so coarsening or abnormal grain growth takes place. Apparently, large grains appear in **Figures 3(b)-(d)**. **Figure 5(b)** shows the MU variation with temperature, *i.e.*, it decreases rapidly with a temperature increase from 1100˚C to 1120˚C but remains almost constant with a further temperature increase.

The size distribution ($G(d)$) of the γ-phase grains under different solution conditions is shown in **Figure 6** and **Figure 7** where $G(d) = N(d, \Delta d)/N_{total}$, d is the individual grain diameter, and $N(d, \Delta d)$ represents the number of the grains
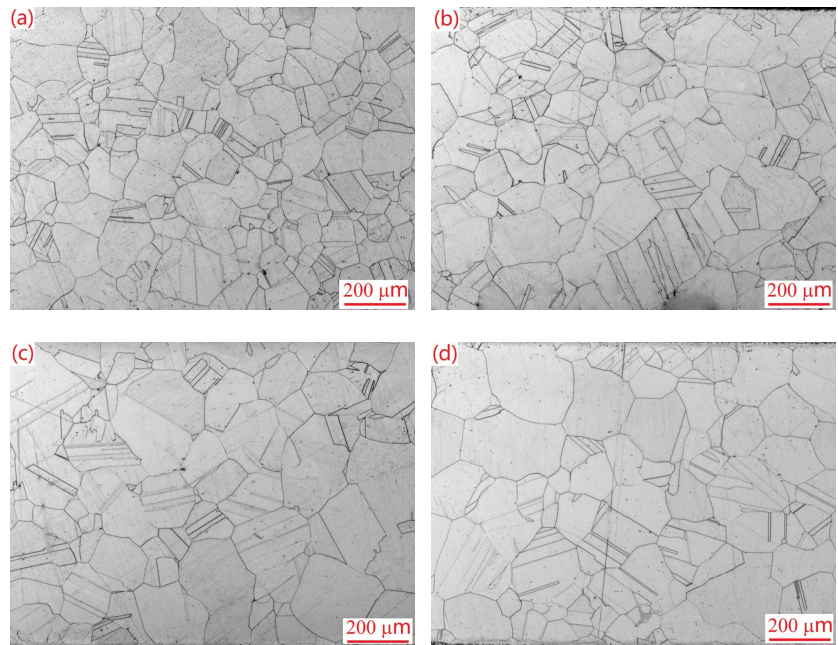
Figure 4. Microstructural evolution of the GH4099 superalloy solution-treated at 1140˚C for (a) 15, (b) 30, (c) 45, and (d) 60 min.
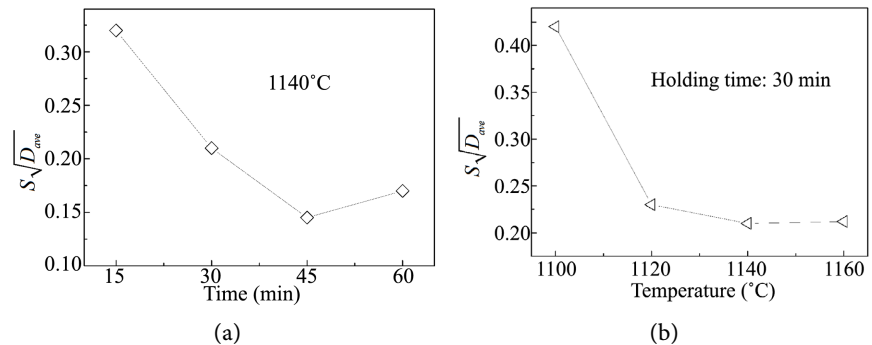

Figure 5. Variation of microstructural uniformity with (a) solution time and (b) temperature.

in a range of $d \pm \Delta d$ with $\Delta d = 20$. The size distribution is sensitive to solution time. In **Figure 7(a)**, the fraction of grains with the size in a range of 140 - 200 mm is very small. The fraction of large grains and the average grain size increase with solution time, as shown in **Figure 7(b)**. **Figure 7(c)** and **Figure 7(d)** represent the grain size distribution at a solution time of 30, 45 and 60 min, respectively. The microstructure becomes more uniform, and the fraction of grains with a size close to the average value is large.

3.2. Grain Growth Kinetics

The main theoretical approach to modeling grain coarsening or Ostwald ripening was developed by Lifshitz and Slozov [16] and Wagner [17] (LSW theory), who predicted that the average grain radius r increases with time t according to the following relationship:
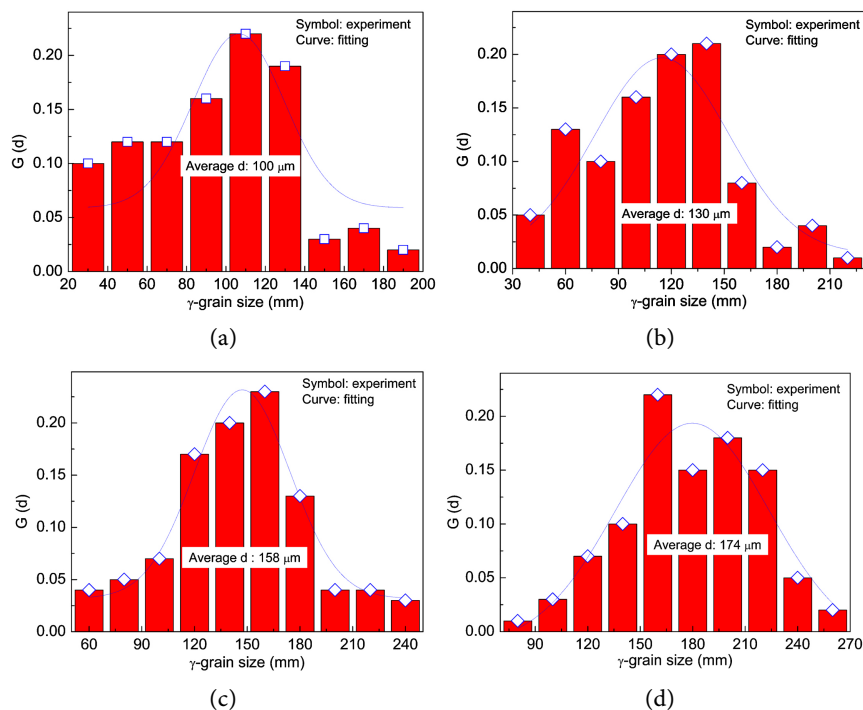
Figure 6. Grain size distribution of γ-phase at (a) 1100˚C, (b) 1120˚C, (c) 1140˚C, and (d) 1160˚C for 30 min.
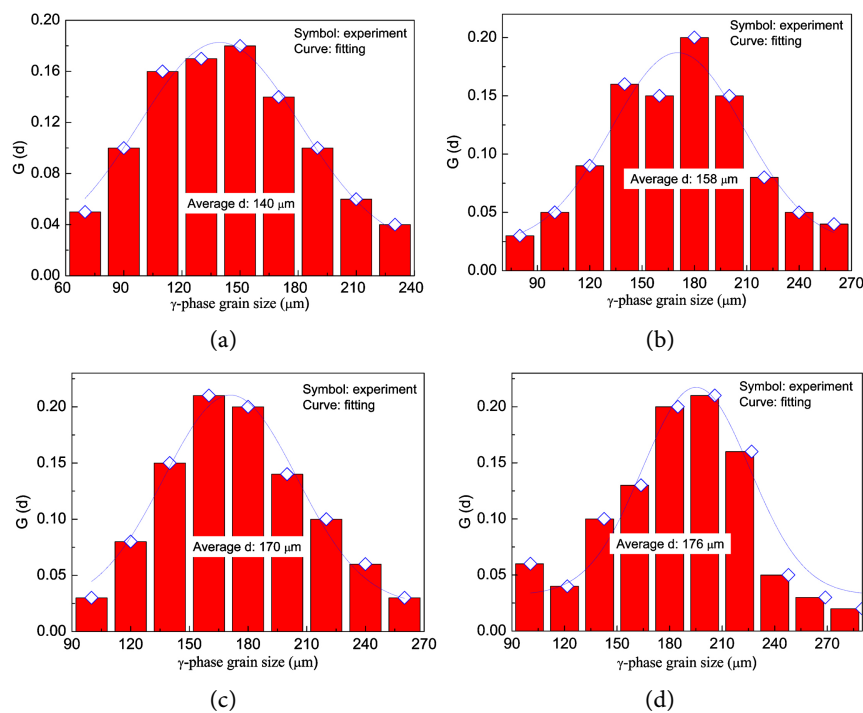

Figure 7. Grain size distribution of γ-phase at 1140˚C for (a) 15, (b) 30, (c) 45, and (d) 60 min.

$$r^n - r_0^n = K_{\text{grow}}t = K_0 \exp\left(-\frac{Q_{\text{act}}}{RT}\right)t \tag{3}$$

where r and r_0 are the average grain radius and the initial value, respectively. K_{grow} is coarsening rate constant, K_0 is material constant, R is gas constant, and T is the absolute temperature. n is the coarsening index, representing different coarsening mechanisms. The parameter n can be 5, 4, 3, or 2 depending on the coarsening mechanism: diffusion via dislocation cores ($n = 5$), along grain boundaries ($n = 4$), through the lattice ($n = 3$), or across a particle-matrix interface ($n = 2$) [18] [19] [20]. The n value needs to be determined experimentally to investigate the coarsening mechanism of the GH4099 superalloy. The n at different temperatures could be deduced by plotting the functional form of $r^n - r_0^n$ vs. t for various values of n, as shown in **Figure 8**. At 1100°C, when n is equal to 5 (see **Figure 8(a)**), the fitting curve is close to being a line; moreover, the correlation coefficient (COE) and slope error of the fitting line are 0.998% and 2.1%, respectively, which means that the value of $n = 5$ could satisfy a linear relationship. Similarly, at 1120°C (**Figure 8(b)**), 1140°C (**Figure 8(c)**) and 1160°C (**Figure 8(d)**), the values of n are close to 5.2, 5.2, and 5.1, respectively, assuming a linear relationship between $r^n - r_0^n$ and t.

The n value at temperatures from 1100°C to 1160°C is close to 5. Thus, the grain coarsening process of the GH4099 superalloy is considered to be controlled by solute diffusion through the dislocation cores. According to Equation (3), the value $K_0 \exp(-Q_{act}/RT)$ is equal to the slope of the fitting line, and the Q_{act} value is assumed to be the same at these temperatures. Thus, Q_{act} can be deduced as 311.7 kJ/mol. The calculated value is higher than the reported activation energies for the γ' coarsening in a Ni matrix (240 - 270 kJ/mol) [12] [14] [18].
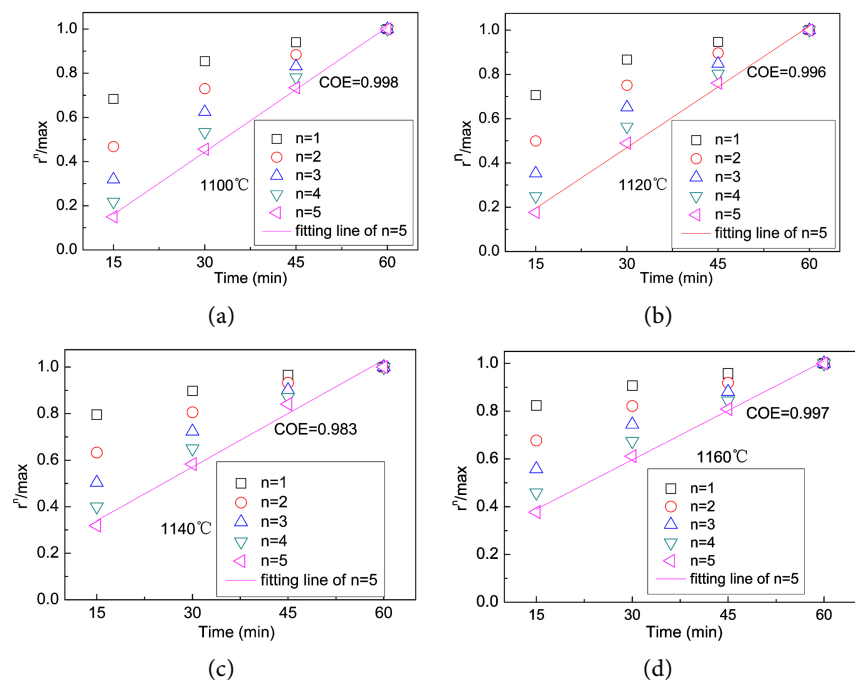

Figure 8. Linear relationship between $r^n - r_0^n$ and t at temperatures of (a) 1100°C, (b) 1120°C, (c) 1140°C, and (d) 1160°C.

3.3. Mechanical Properties

The mechanical properties of the GH4099 superalloy solution-treated at different conditions were tested, and the corresponding values, such as $R_{p0.2}$, R_m, and A_f, are listed in **Table 2**. The solution temperature has a significant effect on strength and ductility. The strength ($R_{p0.2}$ and R_m) decreases with the solution temperature, while ductility exhibits an opposite trend. The $R_{p0.2}$ value decreases from 399 to 298 MPa with an increase in solution temperature from 1100°C to 1160°C, R_m decreases from 863 to 743 MPa, while A_f increases from 58% to 73%, as shown in **Figure 9(a)**.

Many factors may contribute to the strength reduction during the solution treatment. They include dislocation annihilation, γ-grain growth, γ' coarsening, and an increase in solid solubility. In this study, there is no deformation before or after the heat treatment. Thus, no dislocations are produced in the GH4099 samples, so the effect of dislocation annihilation on the strength reduction is
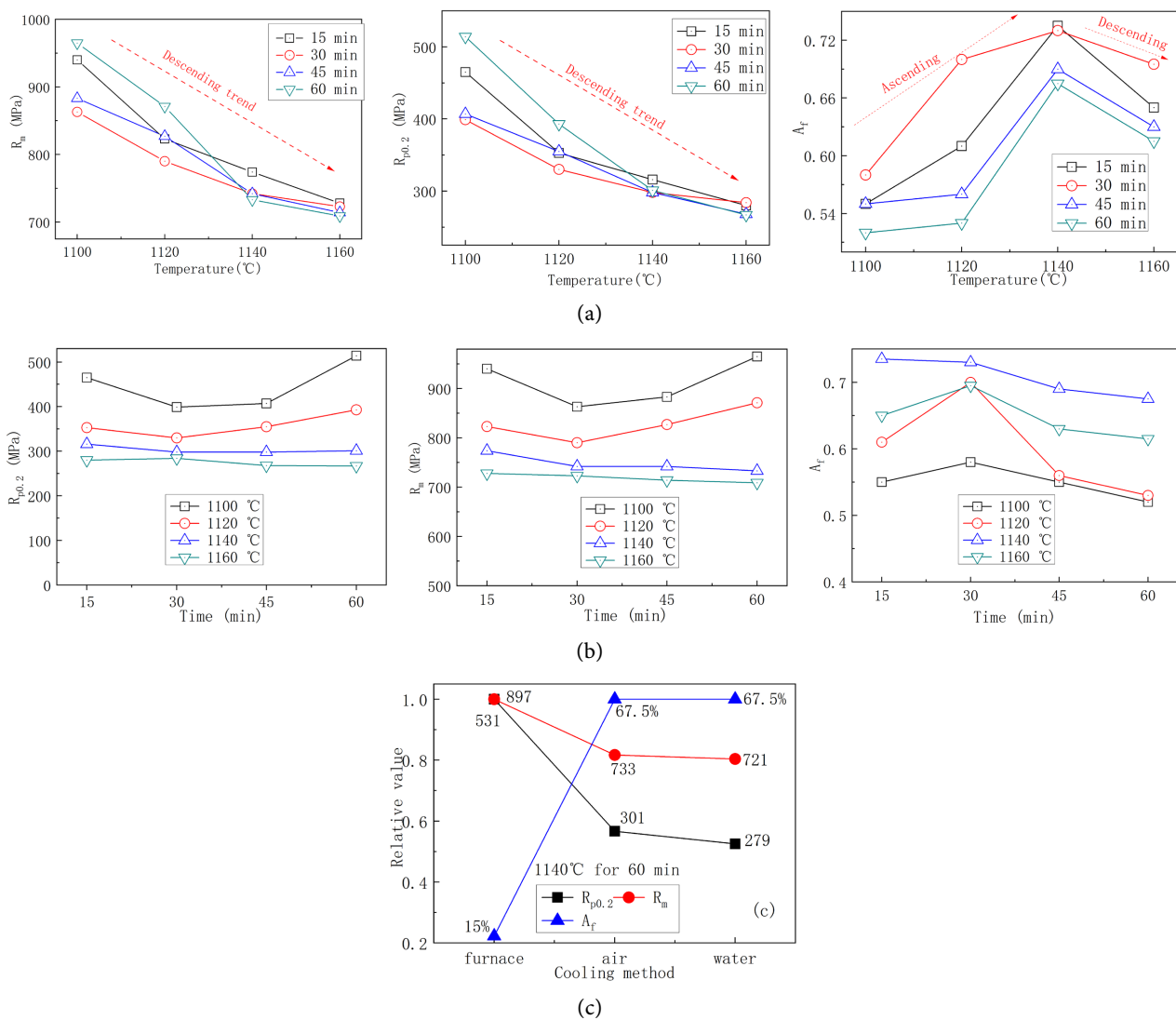

Figure 9. Variation of strength and ductility with (a) solution temperature, (b) time, and (c) cooling method.

Table 2. Tensile properties ($R_{p0.2}/R_m/A_f$) of GH4099 at different temperatures and times followed by air cooling.

Temperature (°C)	Time (min)			
	15	30	45	60
1100	465/940/55%	399/863/58%	407/883/56%	514/965/52%
1120	353/823/61%	330/790/70%	355/827/55%	393/871/53%
1140	316/774/73.5%	298/742/73%	298/742/69%	301/733/67.5
1160	280/728/65%	284/743/69.5%	268/714/63%	267/709/61.5

negligible. The grain sizes of g and γ' phases increase with the solution temperature. The effect of μ

$$\sigma = \sigma_0 + \frac{k_y}{\sqrt{d_m}} \tag{4}$$

where s_0 is the yield strength of a single crystal, k_y is the Hall-Petch coefficient (a value of 750 MPa mm$^{1/2}$ used in many works for nickel-based superalloy) [21] [22], and d_m is the average grain diameter. Thus, the stress reduction caused by grain growth can be expressed as follows:

$$\Delta\sigma_{GBS} = k_y \left(\frac{1}{\sqrt{d_m|_{T_1}}} - \frac{1}{\sqrt{d_m|_{T_2}}} \right) \quad (T_2 > T_1) \tag{5}$$

where $\Delta\sigma_{GBS}$ is the stress reduction, $d_m|_{T_2}$ and $d_m|_{T_1}$ are average sizes at solution temperatures of T_2 and T_1, respectively. The average grain diameter increases from 100 to 174 μm when the solution temperature increases from 1100°C to 1160°C, so the yield strength reduction is calculated to be about 40 MPa. The Hall-Petch effect contribution to the total reduction of $R_{p0.2}$ is 40%. The variation of solid solubility with solution temperature has a significant effect on strength reduction. At 1100°C, the solid solubility of W, Mo, and Co is relatively low, causing a severe lattice distortion of γ-phase and resulting in significant solid-solution strengthening. Thus, the values of $R_{p0.2}$ and R_m are relatively high. The solid solubility of these elements in the γ-matrix increases with the solution temperature. As a result, the lattice distortion is weaker, and the effect of the solid-solution strengthening diminishes. Finally, the strength of the GH4099 superalloy reduces as well.

The effect of solution time on the strength and ductility is also addressed, **Figure 9(b)**. Comparing with **Figure 9(a)**, the variation of $R_{p0.2}$, R_m, and A_f with time is very small. The reduction rates of $R_{p0.2}$ and R_m are only 4.7% and 5.2%, respectively, and A_f retains nearly the same value of 70%. This is because the GH4099 superalloy is solid-solution strengthened, and the solid solubility remains the same at a fixed temperature with increasing time. Moreover, the grain size of γ-phase exhibits a little change with time at a fixed temperature, so the effect of grain boundary strengthening on the strength and ductility is also small.

Therefore, the values of $R_{p0.2}$, R_m, and A_f nearly remain the same during the solution holding stage, although these values exhibit small fluctuations.

Figure 9(c) depicts the significant change in $R_{p0.2}$, R_m, and A_f with the cooling method. In furnace cooling, the values of $R_{p0.2}$ and R_m are 531 and 897 MPa, respectively, way larger than those in **Figure 9(a)** and **Figure 9(b)**, while the A_f value is very small (only 15%). When the cooling changes from furnace cooling (a cooling rate of 1°C/min) to air cooling (a cooling rate of 100°C/min) [23], both $R_{p0.2}$ and R_m decrease rapidly to 301 and 733 MPa, respectively, but A_f increases to 67.5%. With a further increase in the cooling rate to 8000°C/min in water quenching [23], strength and ductility fluctuate nearly remain the same. For the furnace cooling, a very slow cooling rate of 1 °C/min can easily cause the precipitation of γ' phase (Ni$_3$ (Al, Ti)), δ phase (Ni$_3$Nb), and carbides along the γ-grain boundaries and coarsening [24]. Usually, these large precipitates are very hard and brittle. On the one hand, these hard phases/particles may play a vital role in locking or pinning dislocation motions during deformation, which results in the improvement of $R_{p0.2}$ and R_m. On the other hand, due to the precipitation of these brittle phases in the zone of grain boundaries, an intense stress concentration could appear around these zones. Simultaneously, the binding force between neighboring grains becomes weaker, so the material becomes very brittle. Moreover, these hard and brittle particles act as nucleation sites and facilitate the crack propagation, yielding a brittle fracture and finally reducing ductility. The fracture morphology and composition analysis can support this conclusion, which will be discussed in the following section.

3.4. Fracture Morphology and Mechanism

3.4.1. Effect of Solution Temperature

The fracture surfaces of the tensile specimens are investigated using SEM to understand the effect of solution temperature on fracture behavior. As can be seen in **Figure 10**, the fracture surfaces show a mixed ductile and brittle fracture mode. All fracture surfaces are covered with dimples, still expressing some differences between them. In **Figure 10(a)**, when the solution temperature is 1100°C, the fracture surface is flat, but some fine shallow dimples and facets can be observed. The ductility is good, and the corresponding elongation is 58%.

As the solution temperature increases to 1120°C, **Figure 10(b)**, the fracture surface exhibits some morphological ups and downs. The dimples are much deeper and nonuniform in size, and the area fraction of facets decreases compared to that in **Figure 10(a)**. These phenomena indicate that the fracture mode gradually changes from mixed to a typical ductile fracture, which agrees with its better ductility of 70% elongation. However, some microvoids can be observed on the fracture surface. The solid solubility of alloy elements increases with the solution temperature, so higher amounts of elements can dissolve into the γ-phase, increasing their contents increase. This promotes the precipitation of the δ phase and carbides from the matrix during the cooling stage. Lin *et al.* [25] provided a detailed description in terms of the formation and development of
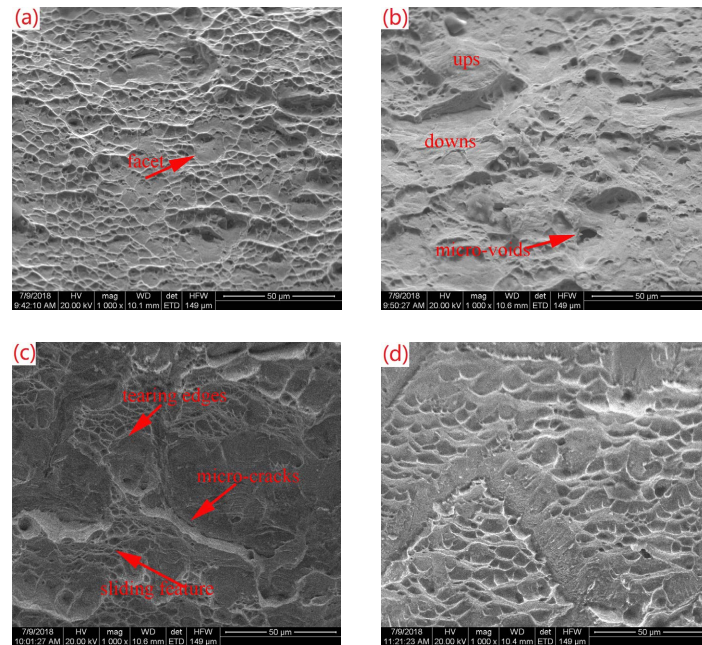
Figure 10. Fracture surfaces of the GH4099 superalloy specimens solution treated at (a) 1100, (b) 1120, (c) 1140, and (d) 1160°C for 30 min.

microvoids. Compared to the γ-phase, the δ-phase, and carbides are relatively hard and brittle. These hard particles impede the dislocation motion during the deformation process, yielding the strain localization and stress concentration around them. As the stress reaches the bond strength of the γ-phase, δ-phase, or carbides, or the breaking limit of δ-phase and carbides, the microvoids nucleate. The microvoids begin to coalesce and extend in the tensile direction with further deformation.

As solution temperature increases to 1140°C, **Figure 10(c)**, large micro-cracks form due to the coalescence of adjacent small dimples in addition to some deep dimples and microvoids distributed on the fracture surface. Some tearing edges appear, and a big fracture step or blade type edge can be observed. Even bigger dimples appear on the fracture surface because of the dimple coalescence. Under such conditions, serpentine sliding features around the dimples become more apparent, *i.e.*, the material experiences a certain degree of plastic deformation after the formation of dimples [25]. Particularly, the serpentine sliding features are getting more and more pronounced, **Figure 10(d)**. The material exhibits a good combination of strength and ductility, consistent with its high values of $R_{p0.2}$, R_m, and A_f.

3.4.2. Effect of Solution Time
Figure 11 shows the effect of solution time on fracture behavior of the GH4099 superalloy. The fracture surfaces of specimens do not change significantly with the solution time. It indicates that the effect of solution time on fracture behavior is not significant compared to the solution temperature. The mixed fracture mode is dominant under these conditions. The fracture surfaces are covered by
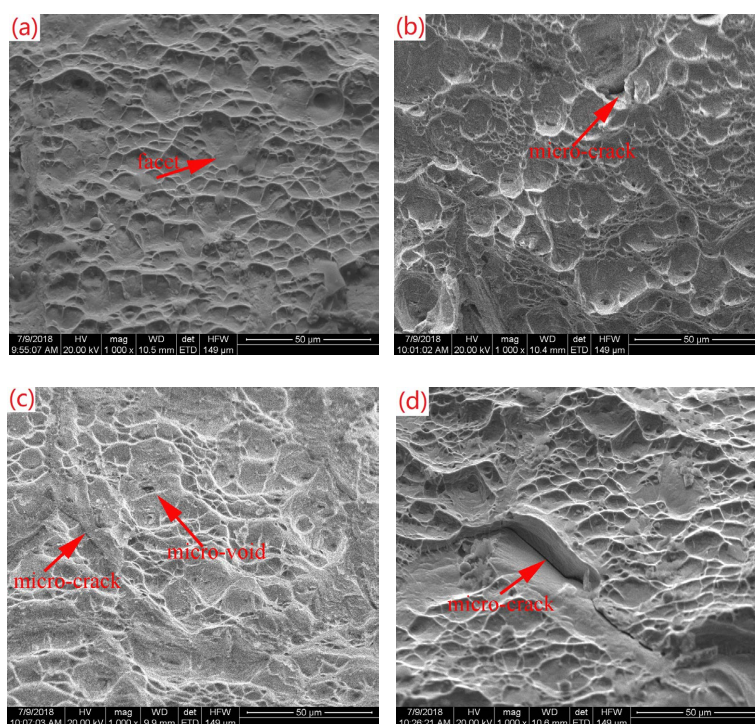
Figure 11. Fracture surfaces of the GH4099 superalloy specimens solution-treated at 1140°C for (a) 15, (b) 30, (c) 45, and (d) 60 min.

many shallow dimples and a few facets. As the solution time prolongs, **Figure 11(b)**, many deep dimples become nonuniform in size compared to those at 1140°C for 15 min, **Figure 11(a)**. Apparent serpentine sliding features occur around the dimples, originating from the new sliding process on the free surface of dimples [23]. However, the intergranular facets are still visible. Some micro-cracks and microvoids appear on the surface, deteriorating the plastic deformation capability of the superalloy. Thus, the strength and ductility of the GH4099 superalloy solution treated at 1140°C for 30 min are close to those for 15 min, which is supported by the variation of $R_{p0.2}$, R_m, and A_f values with the solution time in **Figure 9(b)**. Dimples, serpentine sliding lines, some tearing edges, intergranular facets, micro-cracks, and voids are still distributed on the fracture surfaces with a further increase of solution time. It indicates the fracture mode exhibits a mixed brittle and ductile behavior. The change of the material plasticity with solution time is little.

3.4.3. Effect of Cooling Method

The effect of the cooling method on the fracture behavior is significant, **Figures 12(a)-(c)**. The fracture behavior varies from a mixed brittle and ductile mode to a complete brittle mode. The specimens are water-quenched or cooled in air. Their fracture surfaces exhibit similar characteristics, such as deep dimples with different sizes, serpentine sliding lines, and intergranular facets. The values of $R_{p0.2}$, R_m, and A_f after water quenching matched those after cooling in air. However, when the specimen is subjected to furnace cooling, the fracture surface is
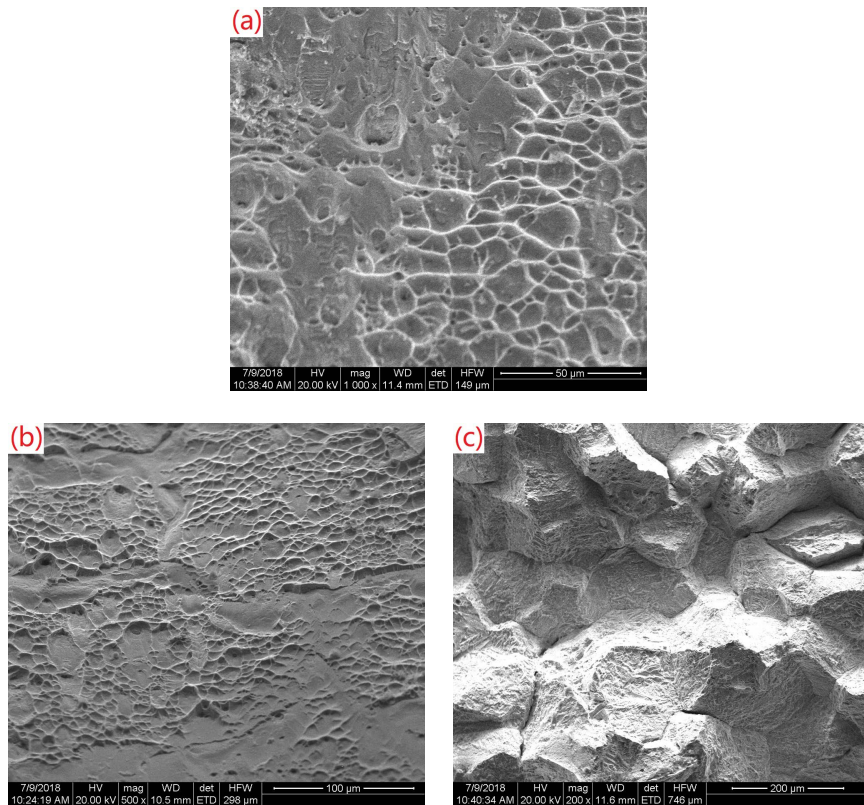
Figure 12. Fracture surfaces of the GH4099 superalloy specimens solution-treated at 1140˚C for 60 min followed by (a) water quenching, (b) air cooling, and (c) furnace cooling.

completely different, showing a typical brittle intergranular fracture mode. The fracture surface is covered by intergranular facets without any dimples. **Figure 12(c)** shows that the γ-phase grain size is very large and nearly exceeds 150 μm because of the apparent growth or coarsening. Moreover, the grain boundaries of the γ-phase become very brittle, and the bonding strength decreases. The nickel-based superalloys' fracture behavior is directly dependent on the relative strength between grain interior and grain boundaries [25]-[30]. For the specimens subjected to furnace cooling, the cooling rate is very slow (about 1˚C/min), and there is enough time for precipitation of various hard and brittle precipitates or carbides from the matrix phase. These hard and brittle particles pin or lock dislocations in the grain boundaries, yielding a high stress concentration. When the stress exceeds the bonding strength of grain boundaries, intergranular fracture occurs. In addition, these zones become preferential nucleation sites for micro-voids or micro-cracks due to the precipitates and carbides at the grain boundaries, which deteriorates the grain boundary strength. The coalescence of micro-voids and micro-cracks promotes the formation of cracks and subsequent propagation along grain boundaries with further plastic deformation.

Figure 13 shows the SEM micrographs of the GH4099 superalloy specimens subjected to different cooling methods to determine the precipitates or carbides in the grain boundaries. The SEM micrographs of the alloy subjected to water
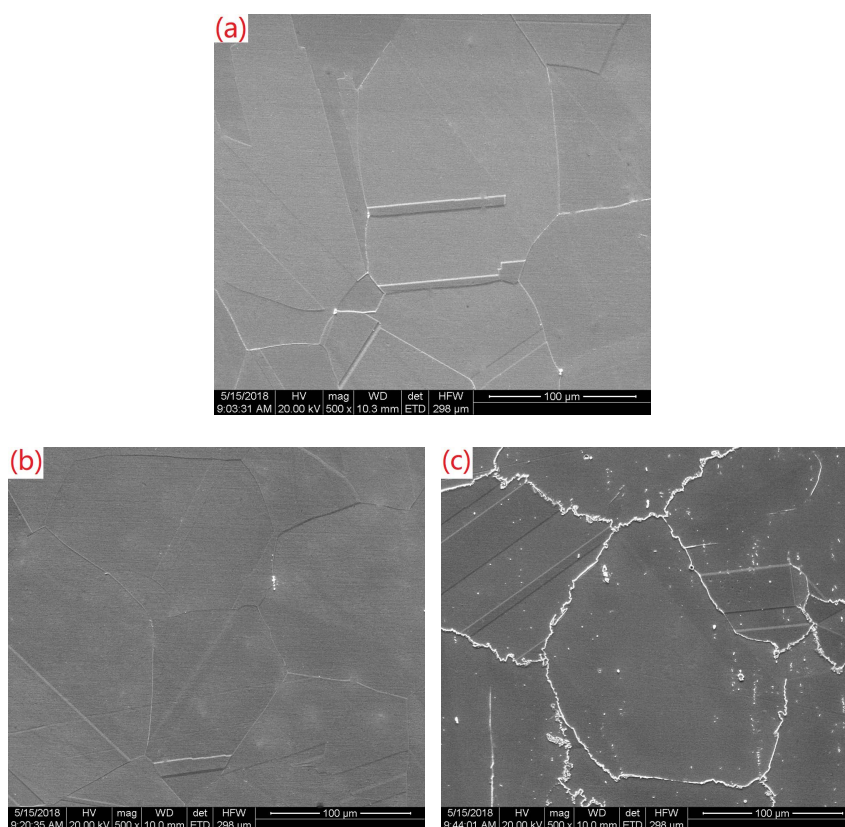
Figure 13. SEM micrographs of the GH4099 superalloy specimens solution-treated at 1140°C for 60 min, followed by (a) water quenching, (b) air cooling, and (c) furnace cooling.

quenching and air cooling are shown in **Figure 13(a)** and **Figure 13(b)**, respectively. The microstructures have similar characteristics. For instance, the gray grain boundaries are relatively straight and clean, and the grain size is in a range of 150 - 170 μm. However, in furnace cooling, **Figure 13(c)**, the microstructure is different from that in **Figure 13(a)** and **Figure 13(b)**, exhibiting serrated grain boundaries where bright precipitation phases appear.

The EDS analysis is used to detect the chemical composition of the matrix, grain boundaries, and precipitates and calculate the weight percentage of each element in the alloy, **Figures 14-16**. **Figure 14(a)** and **Figure 14(b)** show the marked points in the matrix and grain boundaries, respectively. The matrix possesses the same alloy elements as the grain boundary zones. Moreover, the calculated average weight percentage at these points is close to that of the as-received material. It is indicated that there are no secondary phases, such as γ' ($Ni_3(Al, Ti)$), δ (Ni_3Nb), and carbides, precipitating from the matrix phase. The elemental distribution is relatively uniform. Similar results can be observed in **Figure 15**, where the GH4099 superalloy was subjected to air cooling. The matrix contains the same elements as the grain boundaries, and the detected weight percentages in the matrix and grain boundaries are close to those of the as-received material.

Comparison of average composition with as-received		
Element	Average value (wt%)	As received (wt%)
C	01.53	00.06
Al	01.51	02.30
Mo	04.01	04.00
Ti	2.62	01.16
V	00.185	--
Cr	16.13	18.50
Fe	0.46	--
Co	06.17	07.00
Ni	54.03	60.10
W	13.30	06.00
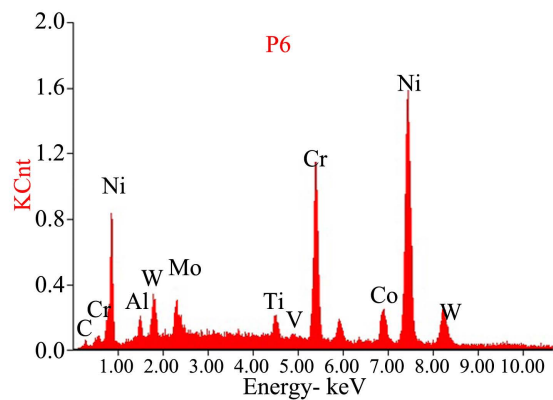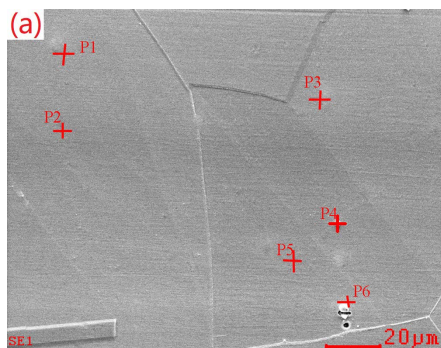
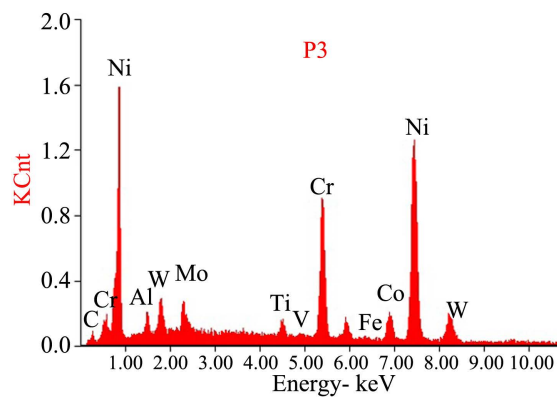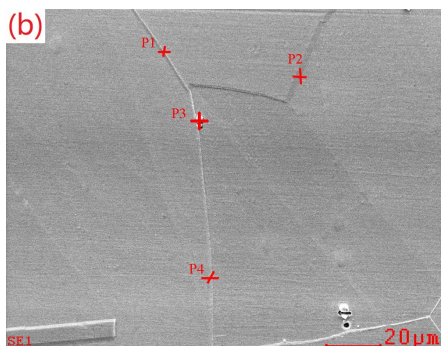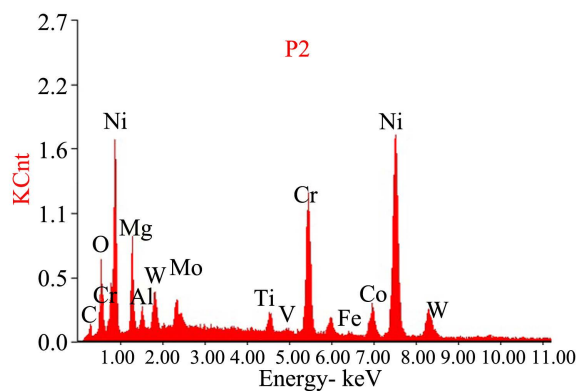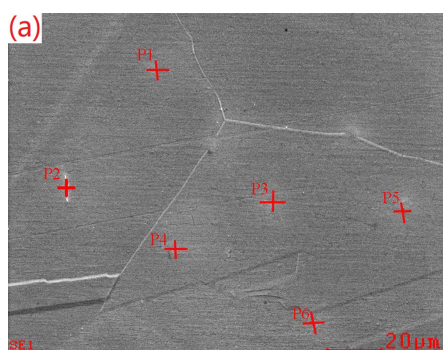| Comparison of average composition with as-received		
Element	Average value (wt%)	As received (wt%)
C	02.66	00.06
Al	01.61	02.30
Mo	04.14	04.00
Ti	02.51	01.16
V	00.135	--
Cr	15.65	18.50
Fe	00.47	--
Co	05.97	07.00
Ni	56.37	60.10
W	10.15	06.00

Figure 14. Elemental composition (in wt%) of marked points in (a) matrix and (b) grain boundaries of the GH4099 superalloy specimens solution-treated at 1140°C for 60 min followed by water quenching.

Comparison of avcragc composition with as-received

Element	Average value (wt%)	As received (wt%)
C	01.03	00.06
Al	01.85	02.30
Mo	04.28	04.00
Ti	02.41	01.16
V	0.028	--
Cr	16.71	18.50
Fe	00.08	--
Co	06.89	07.00
Ni	55.18	60.10
W	08.37	06.00

Comparison of avcragc composition with as-received

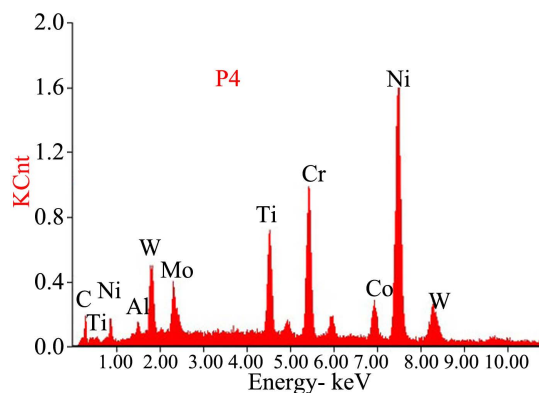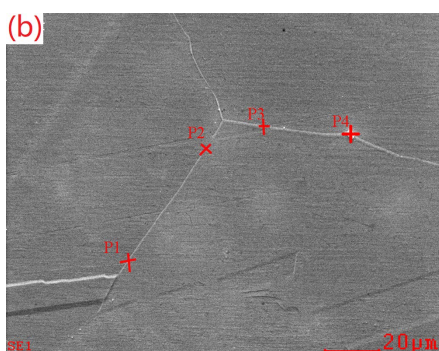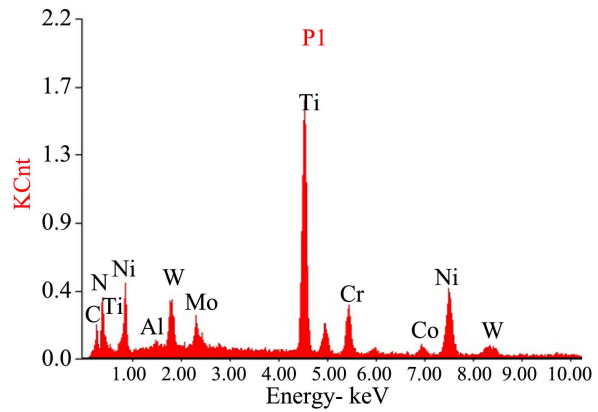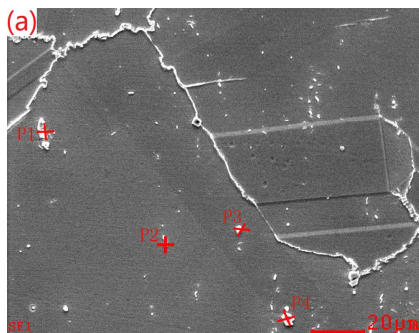| Element	Average value (wt%)	As received (wt%)
C	00.83	00.06
Al	01.26	02.30
Mo	02.72	04.00
Ti	01.58	01.16
V	0	--
Cr	17. 30	18.50
Fe	0	--
Co	05.44	07.00
Ni	57.18	60.10
W	07.01	06.00

Figure 15. Elemental composition (in wt%) of marked points in (a) matrix and (b) grain boundaries of the GH4099 superalloy specimens solution-treated at 1140˚C for 60 min followed by air cooling.
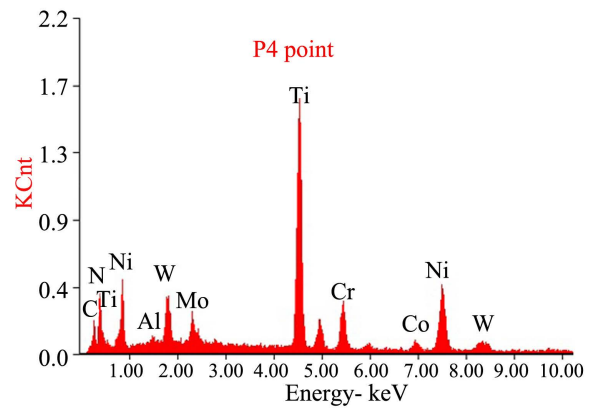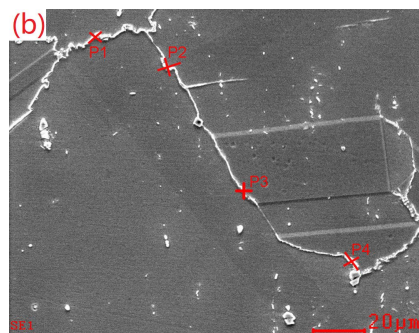
Comparison of average

Element	Average value (wt%)	As received (wt%)
C	00.43	00.06
N	00.22	--
Al	00.37	02.30
Mo	10.14	04.00
Ti	25.93	01.16
Cr	05.69	18.50
Co	02.05	07.00
Ni	45.98	60.10
W	09.19	06.00

Comparison of average composition with
as-received

Element	Average value (wt%)	As received (wt%)
C	0.54	00.06
Al	1.63	02.30
Mo	4.15	04.00
Ti	27.64	01.16
Cr	17.7	18.50
Fe	0	--
Co	2.87	07.00
Ni	22.1	60.10
W	11.7	06.00

Comparison of avcragc composition with
as-received

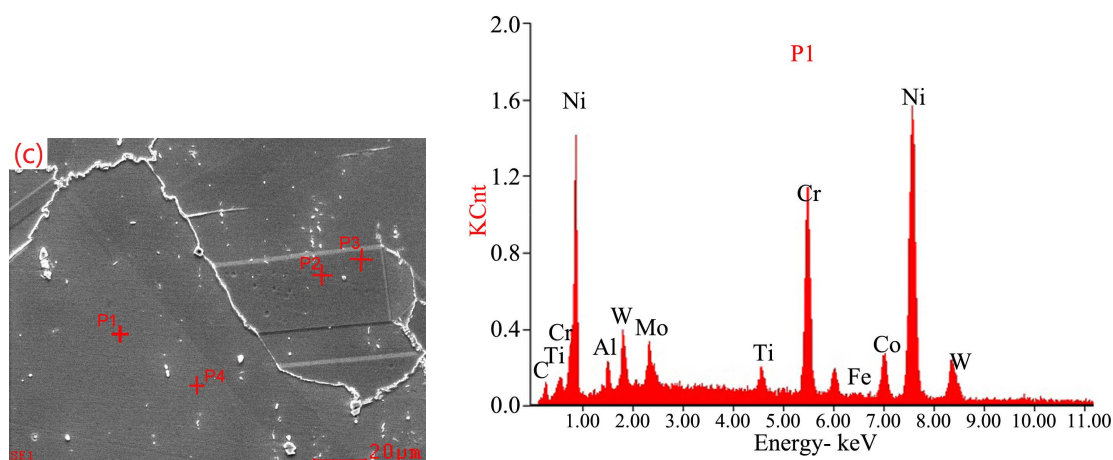| Element	Average value (wt%)	As received (wt%)
C	00.66	00.06
Al	01.49	02.30
Mo	03.72	04.00
Ti	01.46	01.16
Cr	16.89	18.50
Fe	00.27	--
Co	06.24	07.00
Ni	58.07	60.10
W	12.19	06.00

Figure 16. Elemental composition (in wt%) of marked points in (a) bright precipitates in matrix, (b) bright precipitates at grain boundaries, and (c) in the matrix phase without precipitates of the GH4099 superalloy specimens solution-treated at 1140°C for 60 min followed by air cooling.

However, for specimens subjected to furnace cooling, **Figure 16**, the EDS results are different from those in **Figure 14** and **Figure 15**. The bright phases in the matrix and grain boundaries are marked and detected, **Figure 16(a)** and **Figure 16(b)**. The average weight percentage of Ti in the bright precipitate phases is much higher than that in the as-received material (1.16 wt%). The average weight percentages of Ti in the precipitated phase in the matrix and grain boundaries are about 25.93% and 27.64%, respectively. **Figure 16(c)** shows the marked points in the matrix without bright precipitates. The detected element types and weight percentages are close to the as-received material. Thus, it can be deduced that the bright phase may be the γ'-phase, which often appears in superalloys with a small amount of Al and Ti. The γ' phase yields precipitation hardening of the matrix, which in turn reduces the grain boundary strength. Moreover, the precipitates act as potential nucleation sites for cracks, further deteriorating the grain boundary strength. Thus, the grain boundaries become relatively weak, and the cracks propagate along the grain boundaries, causing brittle intergranular fractures.

4. Conclusions

The effects of solution treatments on the microstructural evolution, mechanical properties, and fracture mechanism of the GH4099 superalloy were studied in detail. The main conclusions can be drawn as follows:

1) The average grain size increased from 100 to 174 μm with a temperature increase from 1100°C to 1160°C. The S_v value decreased with temperature and time, implying that the microstructural morphology gradually tended to be uniform and the grain size was approaching the average value. Still, the S_v value gradually increased when holding time was more than 45 min, originating from the γ-grain coarsening or abnormal growth.

2) The influence on the mechanical properties ($R_{p0.2}$, R_m, and A_f) decreased in the order cooling rate, temperature, time. The values of $R_{p0.2}$ and R_m were 531 and 897 MPa, respectively, when the GH4099 was subjected to furnace cooling (with a cooling rate of 1°C/min), but the A_f was only 15%. When the material was subjected to water quenching (with a cooling rate of 8000°C/min) and air cooling (with a cooling rate of 100°C/min), the $R_{p0.2}$ value was in a range from 280 to 301 MPa, and R_m is in a range from 720 to 730 MPa, while A_f rapidly increased to 67.5%.

3) The SEM observation showed that the fracture surfaces changed from a mixed fracture mode (ductile and brittle) to a complete brittle mode when the cooling method changed from water quenching or air cooling to furnace cooling. The EDS analysis indicated the presence of γ′ (Ni$_3$(Al, Ti)) precipitates in the γ-grain boundaries in the furnace cooling stage, which was the main reason for the brittle fracture.

4) Finally, an optimal solution treatment scheme (1140 for °C 30 min followed by air cooling) was proposed for the GH4099 superalloy.

Acknowledgements

Conflicts of Interest

The authors declare no conflicts of interest regarding the publication of this paper.

References

[1] Xia, L.C. (2014) Research on Reasons for Bursting of GH4099 Alloy Bar. *Special Steel Technology*, **20**, 41-46.

[2] Lin, Y.C., Yang, H., Xin, Y.C. and Li, C.Z. (2018) Effects of Initial Microstructures on Serrated Flow Features and Fracture Mechanisms of a Nickel-Based Superalloy.

Materials Characterization, **144**, 9-21. https://doi.org/10.1016/j.matchar.2018.06.029

[3] He, G.D., Lin, Y.C., Chen, S.M., Chen, J., Wen, X.D. and Chen, M.X. (2015) Effect of Pre-Treatment on Hot Deformation Behavior and Processing Map of an Aged Nickel-Based Superalloy. *Journal of Alloys and Compounds*, **649**, 1075-1084. https://doi.org/10.1016/j.jallcom.2015.07.213

[4] He, D.G., Lin, Y.C., Wang, L.H., Wu, Q. and Zu, Z.H. (2019) Influences of Pre-Precipitated δ Phase on Microstructures and Hot Compressive Deformation Features of a Nickel-Based Superalloy. *Vacuum*, **161**, 242-250. https://doi.org/10.1016/j.vacuum.2018.12.043

[5] Lin, Y.C., Yang, H. and Li, L. (2017) Effects of Solutionizing Cooling Processing on Ni_3Nb Phase and Work Hardening Characteristics of a Ni-Fe-Cr-Base Superalloy. *Vacuum*, **144**, 86-93. https://doi.org/10.1016/j.vacuum.2017.07.025

[6] Chen, X.M., Lin, Y.C. and Wu, F. (2017) EBSD Study of Grain Growth Behavior and Annealing Twin Evolution after Full Recrystallization in a Nickel-Based Superalloy. *Journal of Alloys and Compounds*, **724**, 198-207. https://doi.org/10.1016/j.jallcom.2017.07.027

[7] Lin, Y.C. and Chen, X.M. (2011) A Critical Review of Experimental Results and Constitutive Descriptions for Metals and Alloys in Hot Working. *Materials & Design*, **32**, 1733-1759. https://doi.org/10.1016/j.matdes.2010.11.048

[8] Lin, Y.C., Deng, J., Jiang, Y.Q., Wen, D.X. and Liu, G. (2014) Effects of Initial δ Phase on Hot Tensile Deformation Behaviors and Fracture Characteristics of a Typical Ni-Based Superalloy. *Materials Science and Engineering: A*, **598**, 251-262. https://doi.org/10.1016/j.msea.2014.01.029

[9] Anbarasan, N., Bikash, K.G., Prakash, S., Muthukumar, P., Oyyaravelu, R., John, K.F., Kumar, R. and Jerome, S. (2018) Effect of Heat Treatment on the Microstructure and Mechanical Properties of Inconel 718. *Materials Today: Proceedings*, **5**, 7716-7724. https://doi.org/10.1016/j.matpr.2017.11.448

[10] Shi, H., Chen, K., Shen, Z., Wu, J.Q., Dong, X.P., Zhang, L.T. and Shan, A.D. (2015) Twin Boundary Characters Established during Dynamic Recrystallization in a Nickel Alloy. *Materials Characterization*, **110**, 52-59. https://doi.org/10.1016/j.matchar.2015.10.007

[11] Ceena, J., Christer Persson, P. and Magnus, H.C. (2017) Influence of Heat Treatment on the Microstructure and Tensile Properties of Ni-Base Superalloy Haynes 282. *Materials Science and Engineering: A*, **679**, 520-530. https://doi.org/10.1016/j.msea.2016.10.048

[12] Mahboobeh, A., Armin, M., Sama, S., Mohammad, A., Mehdi, S. and Mohammad, H.R. (2018) Effects of Solutioning and Ageing Treatments on Properties of Inconel-713C Nickel-Based Superalloy under Creep Loading. *Materials Science and Engineering: A*, **711**, 195-204. https://doi.org/10.1016/j.msea.2017.11.038

[13] Zhao, S.Q., Xie, X.S., Smith, G.D. and Patel, S.J. (2004) Gamma Prime Coarsening and Age-Hardening Behaviors in a New Nickel Base Superalloy. *Materials Letters*, **58**, 1784-1787. https://doi.org/10.1016/j.matlet.2003.10.053

[14] Chen, M.S., Zou, H.Z., Lin, Y.C., Li, B.H. and Yuan, Q.W. (2018) Effects of Annealing Parameters on Microstructural Evolution of a Typical Nickel-Based Superalloy during Annealing Treatment. *Materials Characterization*, **141**, 212-222. https://doi.org/10.1016/j.matchar.2018.04.056

[15] Masoumi, F., Jahazi, M., Shahriari, D. and Cormier, J. (2016) Coarsening and Dissolution of γ' Precipitates during Solution Treatment of AD730™ Ni-Based Superalloy: Mechanisms and Kinetics Models. *Journal of Alloys and Compounds*, **658**,

981-995. https://doi.org/10.1016/j.jallcom.2015.11.002

[16] Mostafaei, A., Behnamian, Y., Krimer, Y.L., Stevens, E.L., Luo, J.L. and Chmielus, M. (2016) Effect of Solutionizing and Aging on the Microstructure and Mechanical Properties of Powder Bed Binder Jet Printed Nickel-Based Superalloy 625. *Materials & Design*, **111**, 482-491. https://doi.org/10.1016/j.matdes.2016.08.083

[17] Lifshitz, I.M. and Slyozov, V.V. (1961) The Kinetics of Precipitation from Supersaturated Solid Solutions. *Journal of Physics and Chemistry of Solids*, **19**, 35-50. https://doi.org/10.1016/0022-3697(61)90054-3

[18] Wagner, C. (1961) Theorie der Alterung von Niederschlagen durch Umlosen (Ostwald-Reifung). *Zeitschrift für Elektrochemie*, **65**, 581-591.

[19] Johnson, C.H., Richter, S.K., Hamilton, C.H. and Hoyt, J.J. (1999) Static Grain Growth in a Microduplex Ti-6Al-4V Alloy. *Acta Materialia*, **47**, 23-29. https://doi.org/10.1016/S1359-6454(98)00341-3

[20] Wu, C., Yang, H., Li, H.W. and Yang, G.B. (2013) Primary Alpha Grain Coarsening Behavior of Ti-6Al-2Zr-1Mo-1V Alloy in the Alpha + Beta Two-Phase Field. *Journal of Materials Engineering and Performance*, **22**, 2557-2566. https://doi.org/10.1007/s11665-013-0537-8

[21] Campbell, C.E., Boettinger, W.J. and Kattner, U.R. (2002) Development of a Diffusion Mobility Database for Ni-Base Superalloys. *Acta Materialia*, **50**, 775-792. https://doi.org/10.1016/S1359-6454(01)00383-4

[22] Hu, Y.L., Lin, X., Zhang, S.Y., Jiang, Y.M., Lu, X.F., Yang, H.O. and Huang, W.D. (2018) Effect of Solution Heat Treatment on the Microstructure and Mechanical Properties of Inconel 625 Superalloy Fabricated by Laser Solid Forming. *Journal of Alloys and Compounds*, **767**, 330-344. https://doi.org/10.1016/j.jallcom.2018.07.087

[23] Kozar, R.W., Suzuki, A., Milligan, W.W., Schirra, J.J., Sacage, M.F. and Pollock, T.M. (2009) Strengthening Mechanisms in Polycrystalline Multimodal Nickel-Base Superalloys. *Metallurgical and Materials Transactions A*, **40**, 1588-1603. https://doi.org/10.1007/s11661-009-9858-5

[24] Lutjering, G. and Williams, J.C. (2007) Titanium. 2nd Edition, Springer, Berlin.

[25] Lin, Y.C., Yin, L.X., Luo, C.S., He, G.D. and Peng, B.X. (2018) Effects of Initial δ Phase on Creep Behaviors and Fracture Characteristics of a Nickel-Based Superalloy. *Advanced Engineering Materials*, **20**, Article ID: 1700820. https://doi.org/10.1002/adem.201700820

[26] Lin, Y.C., Li, L., He, D.G., Chen, M.S., Liu, G.Q. and Guo, Q. (2017) Effects of Pre-Treatments on Mechanical Properties and Fracture Mechanism of a Nickel-Based Superalloy. *Materials Science and Engineering: A*, **679**, 401-409. https://doi.org/10.1016/j.msea.2016.10.058

[27] Shore, F.M., Morakabati, M., Abbasi, S.M. and Momeni, A. (2014) Hot Deformation Behavior of Incoloy 901 through Hot Tensile Testing. *Journal of Materials Engineering and Performance*, **23**, 1424-1433. https://doi.org/10.1007/s11665-014-0863-5

[28] Rao, G.A., Kumar, M., Srinivas, M. and Sarma, D.S. (2003) Effect of Standard Heat Treatment on the Microstructure and Mechanical Properties of Hot Isostatically Pressed Superalloy Inconel 718. *Materials Science and Engineering: A*, **355**, 114-125. https://doi.org/10.1016/S0921-5093(03)00079-0

[29] Shore, F.M., Morakabati, M., Abbasi, S.M., Momeni, A. and Mahdavi, R. (2014) Hot Ductility of Incoloy 901 Produced by Vacuum Arc Remelting. *ISIJ International*, **54**, 1353-1360. https://doi.org/10.2355/isijinternational.54.1353

[30] Kaupp, G. (2020) Indentation onto Stishovite (SiO$_2$), MgO, and a Covered Superalloy: "Pop-In" Repair, Phase-Transition Onsets, Polymorph Energies, and Transition-Energies. *Advances in Materials Physics and Chemistry*, **10**, 77-95.
https://doi.org/10.4236/ampc.2020.103007